nature materials

LETTERS

| DOI: 10.1038/NMAT4581

Probing disorder in isometric pyrochlore and related complex oxides

Jacob Shamblin[1,2], Mikhail Feygenson[3], Joerg Neuefeind[3], Cameron L. Tracy[4], Fuxiang Zhang[5], Sarah Finkeldei[6], Dirk Bosbach[6], Haidong Zhou[2], Rodney C. Ewing[4] and Maik Lang[1]*

There has been an increased focus on understanding the energetics of structures with unconventional ordering (for example, correlated disorder that is heterogeneous across different length scales[1]). In particular, compounds with the isometric pyrochlore structure[2], $A_2B_2O_7$, can adopt a disordered, isometric fluorite-type structure, $(A,B)_4O_7$, under extreme conditions[3–7]. Despite the importance of the disordering process there exists only a limited understanding of the role of local ordering on the energy landscape. We have used neutron total scattering to show that disordered fluorite (induced intrinsically by composition/stoichiometry or at far-from-equilibrium conditions produced by high-energy radiation) consists of a local orthorhombic structural unit that is repeated by a pseudo-translational symmetry, such that orthorhombic and isometric arrays coexist at different length scales. We also show that inversion in isometric spinel occurs by a similar process. This insight provides a new basis for understanding order-to-disorder transformations important for applications such as plutonium immobilization[4], fast ion conduction[8], and thermal barrier coatings[9,10].

Structural disorder has a profound effect on a material's physical properties. Transport properties are strongly influenced by crystallographic defects which act as scattering centres for quasiparticles, phonons, photons, and so on. For example, structural disorder alters electron transport in graphene[11], photon transport in silicon photonic superlattices[12], flux pinning in superconductors[13], and heat transport properties in thermoelectric materials[14], and thus is used in diverse technological applications. For pyrochlore materials in particular, structural disorder increases catalytic activity in Li–O_2 batteries[15], increases ionic conductivity to levels comparable to yttria-stabilized zirconia[8], and alters radiation resistance, affecting its ability to immobilize radionuclides from spent nuclear fuel[3–5]. Key to these applications is a comprehensive understanding of the origin of the order/disorder transformation.

Complex oxides with aliovalent cations often form superstructures of simpler compounds. Pyrochlore[2] and weberite-type[16] oxides, for example, both form supercells of the fluorite structure with ordered cations and constitutional anion vacancies, but differ in the unit cell size/orientation and symmetry. These highly ordered materials are inherently prone to disordering[5], which influences their behaviour under extreme conditions. These complex structures cannot incorporate significant defect concentrations without partial or complete loss of long-range order. For pyrochlore, experiments show that a disordered phase forms at equilibrium when cations are similar in size (the ratio of cation ionic radii $(r_A/r_B) < 1.46$; ref. 2). This process is governed by the thermodynamics of disordering and the energetics of defect formation, which increases with r_A/r_B (refs 3,17,18). Conventional diffraction techniques characterizing the average structure demonstrated that the order/disorder transformation involves antisite defects, wherein A- and B-site cations randomly exchange positions, and anion Frenkel pairs leading to randomized oxygen vacancies[5–7]. On average, the disordered structure is therefore analogous to the mineral fluorite, with a single cation and anion site. The pyrochlore has essentially lost its superstructure and the unit cell parameter is reduced by 1/2. However, recent studies probing the local structure on disordered fluorite materials have revealed evidence of nonrandom distortions at the nanoscale. For example, whereas the average coordination number (CN) is 7 for both cations in disordered fluorite, reverse Monte Carlo (RMC) analysis from neutron total scattering[19] and X-ray absorption experiments[20,21] have shown that the B-site cation CN (6-coordinated in pyrochlore) remains less than that of the A-site cation (8-coordinated in pyrochlore), suggesting that vacancies are still preferentially localized around the B-site cation. It is still unclear, however, from where this local order arises and how it relates to both the fully ordered and disordered phases.

Pyrochlores with heavy A-site cations, such as Ho, offer a unique opportunity to study this order/disorder transformation, as disorder can be induced through cation substitution on the B-site. Neutron diffraction is ideal to characterize the average structure, as it is sensitive to the oxygen sublattice whereas the pair distribution function (PDF) from neutron total scattering probes the local structure. Structural refinement of fully ordered $Ho_2Ti_2O_7$ shows that the local (assessed through PDF, Fig. 1a) and average (assessed through diffraction, Supplementary Fig. 1) structure are both in excellent agreement with the isometric pyrochlore structure ($Fd\bar{3}m$, Fig. 1d). A-site cations (16d) are coordinated with six 48f oxygen atoms and two 8b oxygen atoms. B-site cations (16c) are coordinated with six 48f oxygen atoms and two ordered 8a vacancies. $Ho_2Ti_2O_7$ can be intrinsically disordered to the fluorite-type average structure by substituting the B-site with larger Zr atoms to form $Ho_2Zr_2O_7$, which has a value of r_A/r_B below the stability field of the pyrochlore structure[2]. Evidence of a modulated structure is apparent in neutron diffraction as broad diffuse peaks orders of magnitude lower in intensity than Bragg peaks[1]. These diffuse peaks, which were

---

[1]Department of Nuclear Engineering, University of Tennessee, Knoxville, Tennessee 37996, USA. [2]Department of Physics and Astronomy, University of Tennessee, Knoxville, Tennessee 37996, USA. [3]Chemical and Engineering Materials Division, Spallation Neutron Source, Oak Ridge National Laboratory, Oak Ridge, Tennessee 37831, USA. [4]Department of Geological Sciences, Stanford University, Stanford, California 94305-2115, USA. [5]Department of Earth and Environmental Sciences, University of Michigan, Ann Arbor, Michigan 48109, USA. [6]Forschungszentrum Jülich, Institute of Energy and Climate Research, IEK-6: Nuclear Waste Management and Reactor Safety, 52425 Jülich, Germany. *e-mail: mlang2@utk.edu

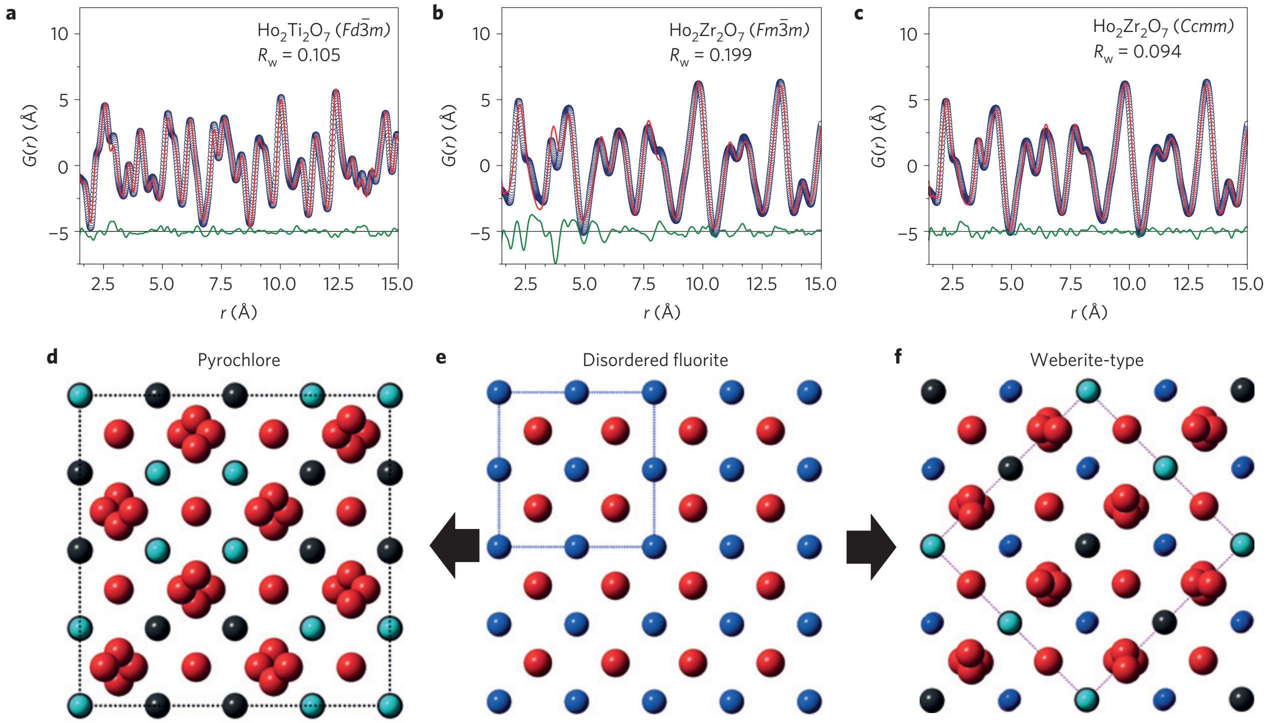

Figure 1 | Neutron PDFs and structural models for ordered ($Ho_2Ti_2O_7$) and disordered ($Ho_2Zr_2O_7$) pyrochlore. a, Small-box refinement of the neutron PDF, $G(r)$, as a function of distance, r, using the ordered $Ho_2Ti_2O_7$ pyrochlore structure shown in **d**. Open circles represent experimental data, the solid red line represents the fit obtained through refinement, and the solid green line represents the difference between the experimental data and the refinement. The average and local structures agree well. It should be noted that Ho and Ti have contrasting neutron scattering lengths (7.17 and −3.438 fm respectively) resulting in positive peaks for Ho–O correlations and negative peaks for Ti–O correlations. **b**, Small-box refinement of the neutron PDF for $Ho_2Zr_2O_7$ with the disordered fluorite structure shown in **e**. Although the disordered fluorite model characterizes the average structure in $Ho_2Zr_2O_7$ well, the PDF shows a poor fit locally, particularly below 10 Å, as noted by the difference curve. **c**, Small-box refinement of the neutron PDF for $Ho_2Zr_2O_7$ with the orthorhombic weberite-type structure shown in **f**. The local structure is captured very well. The refinement range of **a**–**c** was 1–15 Å. **d**–**f**, Structural relations between the pyrochlore (**d**), disordered fluorite (**e**) and weberite-type (**f**) arrangements. Both the pyrochlore and weberite-type structures are supercells of disordered fluorite with unit cell parameters of $a_{PC} = a_{WB} = 2a_{DF}$ and $b_{WB} \approx c_{WB} \approx a_{DF}\sqrt{2}$ (the subscripts refer to pyrochlore, weberite-type and disordered fluorite respectively). Red spheres represent oxygen sites that are fully occupied in the pyrochlore and weberite-type structures but 7/8ths occupied in disordered fluorite. Black and cyan spheres represent A- (CN = 8) and B-site (CN = 6) cations, respectively. Blue spheres designate cation site mixing (CN = 7).

absent in $Ho_2Ti_2O_7$, must be discarded as background during the Rietveld refinements[20]. The disordered fluorite model fits well to the diffraction data of $Ho_2Zr_2O_7$ when diffuse contributions are subtracted with the background (Fig. 2). However, this treatment of the background provides no quantitative information regarding the origin of the diffuse scattering; hence, PDF analysis is necessary to study the local crystal structure.

Disorder is readily apparent in the PDF as many distinct peaks in the $Ho_2Ti_2O_7$ data merge into single, broader peaks for $Ho_2Zr_2O_7$ (Fig. 1b). The local structure was initially refined with the average fluorite-type structural model ($Fm\bar{3}m$, Fig. 1e) in which A- and B-site cations randomly occupy 4*a* sites and anions occupy 7/8ths of 8*c* sites. As shown by the substantial deviations from the zero baseline of the difference curve, there are significant mismatches in peak positions/intensities, specifically below 10 Å (about two unit cells), despite a satisfactory fit over longer length scales (Supplementary Table 1). There is also a shoulder at $r = 2.6$ Å that is not captured in the simulated PDF. The ordered pyrochlore structure was also fitted to the experimental data and similarly fails to reproduce the PDF in largely the same areas as the disordered fluorite model (Supplementary Fig. 2). As shown in Fig. 1c, the quality of the fit using the orthorhombic weberite-type model ($Ccmm$, Fig. 1f) is significantly improved as compared with the fluorite-type model. The goodness-of-fit parameter (R_w) is reduced from 0.199 to 0.094 and the entire r-range is modelled accurately. Such a local structure has been proposed for fluorite-type Yb_3TaO_7 (ref. 22), which has a stoichiometry prone to long-range weberite-type ordering[16]. The present PDF data show that this specific local order is exhibited by a broader class of disordered fluorite-derivative oxides, for compositions in which weberite-like ordering has not been previously observed over any length scale.

The weberite-type arrangement maintains a fluorite-derivative superstructure similar to pyrochlore (see arrows in Fig. 1); however, the symmetry is reduced. Cations occupy 4*a*, 4*b* and 8*g* sites, which are in octahedral (6-fold), distorted cubic (8-fold) and distorted mono-capped octahedral (7-fold) coordination, respectively (Supplementary Fig. 3). Anions occupy 16*h* and three 4*c* sites. There remains an ordered vacancy, as in the pyrochlore structure, but it is now located at a fourth 4*c* site (Supplementary Fig. 4). Ho and Zr have similar neutron scattering lengths, making it difficult to distinguish which cation resides on which site. However, many bond lengths become unphysical when Zr is located on 4*b* sites. The weberite-type structure is formed from distortions of alternating layers in the pyrochlore structure, as both cations become 7-coordinated within these layers (Supplementary Fig. 3). Zr and Ho therefore probably occupy octahedral (4*a*) and distorted cubic (4*b*) sites, respectively (analogous to the pyrochlore orientation), and share occupancy of the mono-capped octahedral layers (Supplementary Fig. 4). Total site multiplicity is reduced from 96 to 48 (compared with 12 in fluorite) such that the weberite-type structure can be considered a disordered derivative of the pyrochlore structure. This is in agreement with

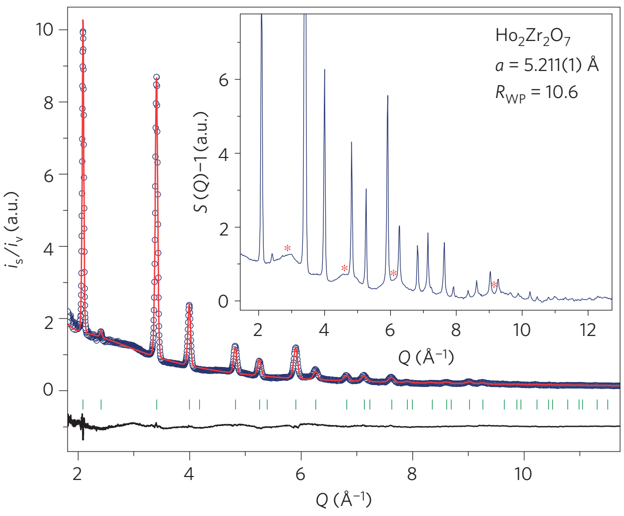

Figure 2 | Neutron powder diffraction pattern (open circles) of $Ho_2Zr_2O_7$ refined with the isometric disordered fluorite structure (solid red line). The black line represents the difference between the experimental and calculated pattern. Vertical ticks denote refined Bragg peak positions. The differing local structure results in diffuse peaks shown in the total scattering structure function (inset, designated with red asterisks) that must be refined with the background or ignored if a disordered fluorite structure is assumed. Q, momentum transfer of the scattered neutrons; $S(Q)$, total scattering structure function; i_s/i_v, scattering intensity from the sample normalized to the scattering intensity from vanadium; R_{WP}, goodness-of-fit parameter obtained through Rietveld refinement.

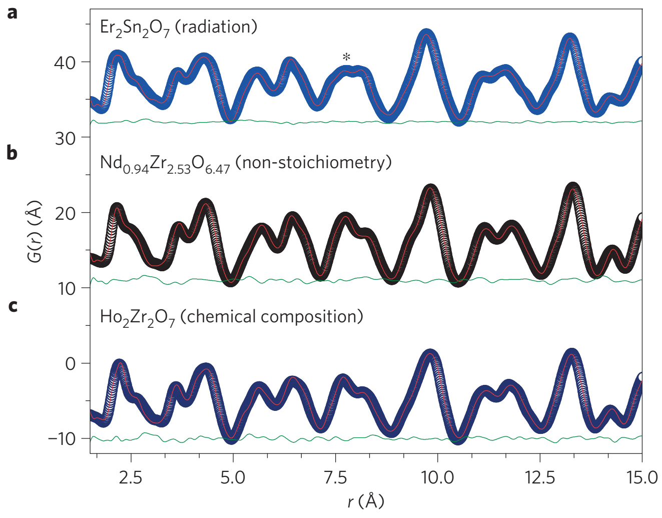

Figure 3 | Comparison of neutron PDFs (open circles) for intrinsically and extrinsically disordered pyrochlores. Disorder was achieved by irradiation with 2.2 GeV Au ions ($Er_2Sn_2O_7$) (**a**), non-stoichiometry ($Nd_{0.94}Zr_{2.53}O_{6.47}$) (**b**) and chemical composition ($Ho_2Zr_2O_7$) (**c**). The green line represents the difference between the experimental data (open circles) and the refinement (red line). Data from all three samples fit well to the weberite-type structural model (solid red line), demonstrating the generality of this disordering mechanism. Ion-irradiated $Er_2Sn_2O_7$ exhibits one visible difference, as denoted by an asterisk, that is probably due to residual pyrochlore contributions from unirradiated portions of the sample or additional defects produced from ionizing radiation. The refinement range was 1–15 Å for all three samples. $G(r)$, pair distribution function; r, radial distance.

RMC (ref. 19) and X-ray absorption[20] experiments showing that although disorder is accompanied by an increase in B-site CN and a decrease in A-site CN, the two are not equivalent, as would be the case with disordered fluorite local ordering, having a CN of 7. Redox effects in disordered titanate pyrochlores could further alter local coordination, as previous X-ray absorption experiments suggest that the titanium CN reduces (at least partially) from 6 to 5 (refs 21,23).

Although $Ho_2Ti_2O_7$ can be described as pyrochlore in terms of both local and average structure, disordered $Ho_2Zr_2O_7$ shows distinct regimes over different length scales: the average structure is consistent with isometric disordered fluorite whereas the local structure is weberite-type. This indicates that the average structure must be assembled by aperiodic, three-dimensional modulation of local structural units, inevitably forming a regime where the weberite-type structure no longer applies. Although the PDF can be accurately modelled as weberite-type from 1.5 to 15 Å, the intensity and position of the peaks below 5 Å are no longer reproducible if the fit range is expanded to 1.5–25 Å. The difference curve more closely resembles that of the disordered fluorite model (Supplementary Figs 5 and 6), suggesting that the weberite-type structure is valid only for one to two unit cell repeats. Thus, the present data clearly show that disordering of pyrochlore oxides is complex, involving two distinct mechanisms on different length scales: the ordered local pyrochlore structure transforms into orthorhombic weberite-type units, and aperiodic modulation of these local units yields an average isometric disordered fluorite structure.

Ordered pyrochlores were also disordered by irradiation with high-energy heavy ions ($Er_2Sn_2O_7$) and modification of the $A_2B_2O_7$ stoichiometry ($Nd_{0.94}Zr_{2.53}O_{6.47}$), such that the A-site is partially occupied by B-site cations (Fig. 3). Independently of the starting composition and means of disordering, the local structure can be in each case accurately refined with the weberite-type phase (Supplementary Tables 1 and 2); the fluorite phase is consistent only with the average, disordered structure. Thus, the same disordering mechanism operates independently of the source of the disorder (intrinsic or extrinsic).

The discovery of the local weberite-type structure in fully disordered pyrochlore is essential to the description of atomic-scale phase transformations of such materials under extreme conditions. Atomistic simulations almost exclusively adopt a fully disordered fluorite model or focus on single defect energies to predict physical properties such as radiation stability and disordering temperature[3,17,24]. In general, this approach has reproduced similar trends to those in experiment; however, the heterogeneous disorder presented here undoubtedly affects the energy landscape and needs to be accounted for to fully understand the order-to-disorder transition. For example, cation antisite and anion Frenkel pairs are energetically very expensive in $Er_2Sn_2O_7$ (ref. 17). However, previous experiments have shown that this compound forms the fluorite phase under particle radiation[18], which would be unexpected if local ordering did not play a key role in the order-to-disorder transition.

This transition also affects high-pressure behaviour of many pyrochlore compositions. At room temperature and a critical pressure of ∼20 GPa, isometric pyrochlore transitions to an orthorhombic, cotunnite-like phase[6,7], which transforms to the disordered fluorite structure upon quenching. Although this phase transformation has been studied in detail, the structural relationships among the different phases and the associated pathways are not well understood. This new insight into heterogeneous disorder provides the atomic-scale relationship between the three structures and a potential transformation mechanism. The cotunnite-like (*Pnam*) structure is a non-isomorphic subgroup of the orthorhombic (*Ccmm*) local coordination that has been here shown to exist in disordered fluorite compounds. Analogous to chemical composition, non-stoichiometry, and radiation, pressure probably disorders the local pyrochlore structure into orthorhombic units. The applied pressure, however, hinders structural modulations, resulting in long-range

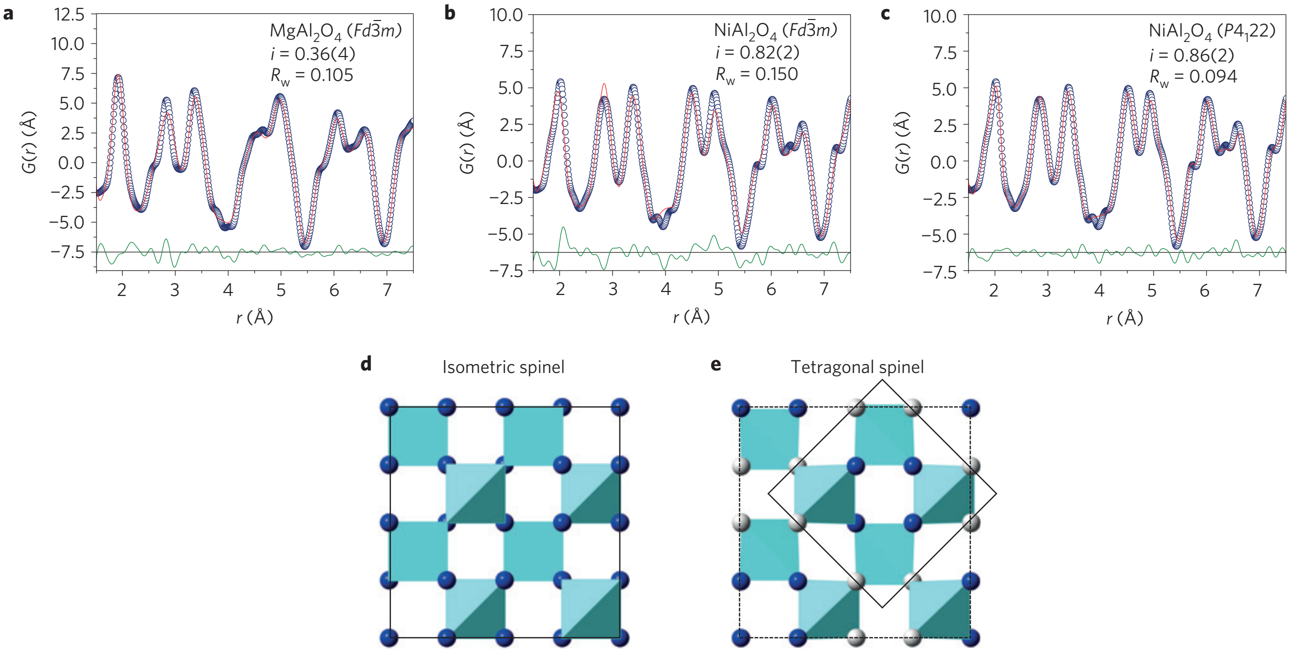

Figure 4 | Neutron PDFs and structural models for normal ($MgAl_2O_4$) and inverse ($NiAl_2O_4$) spinel. a, Small-box refinement of $MgAl_2O_4$ spinel, $G(r)$, as a function of distance, r, using the isometric ($Fd\bar{3}m$ space group) average structure shown in *d*. The refined inversion fraction, i, is 0.36(4). The isometric structure fits reasonably well; however, there is evidence of minor local distortions, as noted by the refined width and height of the peak at 2.8 Å. This is probably due to partial ordering of the Mg/Al atoms occupying octahedral B-sites, as the tetragonal distortion discussed in **c** models this peak accurately (Supplementary Fig. 10). **b**, Refined PDF of $NiAl_2O_4$ spinel using the isometric ($Fd\bar{3}m$ space group) average structure shown in **d**. The refined inversion fraction is 0.82(2). The position and left shoulder of the first peak are not captured through refinement and several other intensities are poorly modelled. **c**, Refined PDF of $NiAl_2O_4$ spinel using the tetragonal distortion ($P4_122$ space group) shown in **e**. The refined inversion fraction is 0.86(2). The shoulder and position of the first peak are now modelled accurately and refined peak intensities now line up favourably with the measured data. All PDFs were refined from 1–10 Å. **d**, Structure of isometric spinel with two cation sites. Cyan polyhedra indicate A-site tetrahedra while blue spheres indicate octahedral B-sites. Inversion is defined as the fraction of Mg (or Ni) atoms that share mixed occupancy of octahedral B-sites with Al. The solid black line delineates the unit cell. **e**, Structure of tetragonal spinel with three distinct cation sites. A-site tetrahedra (cyan polyhedra) are slightly distorted and shifted from their ideal isometric lattice sites, otherwise the A-site sublattice is unchanged from that of the isometric spinel. The B-site sublattice in isometric spinel is split into two separate octahedral sites in the tetragonal distortion (grey and blue spheres). Inversion is defined as the fraction of Ni that share mixed occupancy of 4*a* octahedral sites (grey spheres) with Al. The remaining Ni atoms share occupancy of tetrahedral sites with Al. The 4*b* octahedral sites (blue spheres) are fully occupied by Al. The solid black line delineates the tetragonal unit cell. The unit cell orientation for isometric spinel is shown for reference (dashed black line).

orthorhombic periodicity. Once pressure is released, the long-range structure relaxes into disordered fluorite on average.

Total scattering data on isometric spinel shows that this complex disordering mechanism extends beyond the fluorite system. Many compounds of AB_2O_4 stoichiometry form an isometric spinel structure that, like pyrochlore, can be disordered by changing composition[25], irradiation[26] and temperature/pressure[27,28]. The local (assessed with PDF, Fig. 4a) and average (assessed with diffraction, Supplementary Fig. 7) structure of $MgAl_2O_4$ agree well with isometric spinel (Fig. 4d), although minor distortions appear to be present at 2.8 Å. Unlike $MgAl_2O_4$, $NiAl_2O_4$ forms an inverse spinel structure in which tetrahedrally coordinated A-site cations exchange with nearly half of octahedrally coordinated B-site cations (indicated as $B(AB)O_4$). The octahedral sublattice can therefore be viewed as fully disordered, on average, as A- and B-site cations are 'randomly' distributed across octahedral sites (Supplementary Fig. 8). The PDF, however, shows that this description is not valid locally, as evidenced by the deviations between the measured data and the refinement at low-r (Fig. 4b). The tetragonal spinel phase with three ordered cation sites and a different unit cell orientation (Fig. 4e) agrees well with the PDF (Fig. 4c), indicating the cations are locally ordered within a tetragonal 'unit cell' (Supplementary Fig. 9). This also improves the fit of the peak at 2.8 Å for $MgAl_2O_4$ (Supplementary Fig. 10). This is consistent with Raman spectroscopy measurements on inverse $NiFe_2O_4$ (ref. 29) and agrees with first-principles calculations demonstrating that short-range effects must be included to accurately predict cation inversion tendencies[30]. This relationship is analogous to that of weberite-type/pyrochlore. Just as the pyrochlore is a 2 × 2 × 2 superstructure of fluorite, spinel can be viewed as a 2 × 2 × 2 superstructure of NaCl (ref. 25). Upon disordering, the local 'unit cell' is reduced to an approximately $2 \times \sqrt{2} \times \sqrt{2}$ supercell of its base structure (that is, fluorite or NaCl).

In summary, PDF analysis from neutron total scattering has provided new insight into disorder in isometric complex oxides. In particular, the isometric, fluorite structure in disordered $A_2B_2O_7$ does not exist at the atomic level. These complex oxides consist of local orthorhombic structural units that are pseudo-randomly arranged to form the well-known average disordered fluorite structure. This modulated structure is consistent whether disorder is introduced extrinsically (irradiated $Er_2Sn_2O_7$) or intrinsically ($Ho_2Zr_2O_7$ and $Nd_{0.94}Zr_{2.53}O_{6.47}$). Similar behaviour is observed for spinel inversion, as modulations of a local tetragonal configuration form a disordered isometric structure on average. Understanding the nature of this heterogeneous disorder presents a new basis for the study of structural and physical properties in a broad class of complex oxides. Just as short-range effects have been shown to be computationally necessary in spinel[30], atomistic simulations which neglect local ordering in disordered pyrochlores represent an incomplete approach to fully understand the disordering process.

We have shown, for the first time, that this local order in both pyrochlore and spinel systems does not arise from the ordered, isometric structure, but rather from a smaller unit cell of lower symmetry. This can be used to improve predictions for important properties such as disordering temperature, ionic conductivity and radiation stability.

Methods

Methods and any associated references are available in the online version of the paper.

Received 22 September 2015; accepted 25 January 2016;

References

1. Keen, D. A. & Goodwin, A. L. The crystallography of correlated disorder. *Nature* **521,** 303–309 (2015).
2. Subramanian, M. A., Aravamudan, G. & Rao, G. V. S. Oxide pyrochlores—a review. *Prog. Solid State Chem.* **15,** 55–143 (1983).
3. Sickafus, K. E. *et al*. Radiation tolerance of complex oxides. *Science* **289,** 748–751 (2000).
4. Ewing, R. C., Weber, W. J. & Lian, J. Nuclear waste disposal-pyrochlore ($A_2B_2O_7$): nuclear waste form for the immobilization of plutonium and "minor" actinides. *J. Appl. Phys.* **95,** 5949–5971 (2004).
5. Sickafus, K. E. *et al*. Radiation-induced amorphization resistance and radiation tolerance in structurally related oxides. *Nature Mater.* **6,** 217–223 (2007).
6. Zhang, F. X. *et al*. Phase stability and pressure dependence of defect formation in $Gd_2Ti_2O_7$ and $Gd_2Zr_2O_7$ pyrochlores. *Phys. Rev. Lett.* **100,** 045503 (2008).
7. Zhang, F. X., Lang, M., Liu, Z. & Ewing, R. C. Pressure-induced disordering and anomalous lattice expansion in $La_2Zr_2O_7$ pyrochlore. *Phys. Rev. Lett.* **105,** 015503 (2010).
8. Wuensch, B. J. *et al*. Connection between oxygen-ion conductivity of pyrochlore fuel-cell materials and structural change with composition and temperature. *Solid State Ion.* **129,** 111–133 (2000).
9. Padture, N. P., Gell, M. & Jordan, E. H. Thermal barrier coatings for gas-turbine engine applications. *Science* **296,** 280–284 (2002).
10. Wu, J. *et al*. Low-thermal-conductivity rare-earth zirconates for potential thermal-barrier-coating applications. *J. Am. Ceram. Soc.* **85,** 3031–3035 (2002).
11. Castro Neto, A. H., Guinea, F., Peres, N. M. R., Novoselov, K. S. & Geim, A. K. The electronic properties of graphene. *Rev. Mod. Phys.* **81,** 109–162 (2009).
12. Hsieh, P. *et al*. Photon transport enhanced by transverse Anderson localization in disordered superlattices. *Nature Phys.* **11,** 268–274 (2015).
13. Civale, L. *et al*. Vortex confinement by columnar defects in $YBa_2Cu_3O_7$ crystals—enhanced pinning at high fields and temperatures. *Phys. Rev. Lett.* **67,** 648–651 (1991).
14. Biswas, K. *et al*. High-performance bulk thermoelectrics with all-scale hierarchical architectures. *Nature* **489,** 414–418 (2012).
15. Oh, S. H., Black, R., Pomerantseva, E., Lee, J.-H. & Nazar, L. F. Synthesis of a metallic mesoporous pyrochlore as a catalyst for lithium-O_2 batteries. *Nature Chem.* **4,** 1004–1010 (2012).
16. Rooksby, H. P. & White, E. A. D. Rare-earth niobates and tantalates of defect fluorite-type and weberite-type structures. *J. Am. Ceram. Soc.* **47,** 94–96 (1964).
17. Li, Y. *et al*. Defect formation energies in $A_2B_2O_7$ pyrochlores. *Scr. Mater.* **107,** 18–21 (2015).
18. Lian, J. *et al*. Effect of structure and thermodynamic stability on the response of lanthanide stannate-pyrochlores to ion beam irradiation. *J. Phys. Chem. B* **110,** 2343–2350 (2006).
19. Norberg, S. T. *et al*. Pyrochlore to fluorite transition: the $Y_2(Ti_{1-x}Zr_x)_2O_7$ ($0.0 \leq x \leq 1.0$) system. *Chem. Mater.* **24,** 4294–4300 (2012).
20. Blanchard, P. E. R. *et al*. Does local disorder occur in the pyrochlore zirconates? *Inorg. Chem.* **51,** 13237–13244 (2012).
21. Sanjuan, M. L. *et al*. Raman and X-ray absorption spectroscopy study of the phase evolution induced by mechanical milling and thermal treatments in $R_2Ti_2O_7$ pyrochlores. *Phys. Rev. B* **84,** 104207 (2011).
22. King, G., Thompson, C. M., Greedan, J. E. & Llobet, A. Local structure of the vacancy disordered fluorite Yb_3TaO_7 from neutron total scattering. *J. Mater. Chem. A* **1,** 10487–10494 (2013).
23. Walker, J. D. S., Hayes, J. R., Gaultois, M. W., Aluri, E. R. & Grosvenor, A. P. A case for oxygen deficiency in $Gd_2Ti_{2-x}Zr_xO_7$ pyrochlore-type oxides. *J. Alloys Compd.* **565,** 44–49 (2013).
24. Jiang, C., Stanek, C. R., Sickafus, K. E. & Uberuaga, B. P. First-principles prediction of disordering tendencies in pyrochlore oxides. *Phys. Rev. B* **79,** 104203 (2009).
25. Verwey, E. J. W. & Heilmann, E. L. Physical properties and cation arrangement of oxides with spinel structures I. Cation arrangement in spinels. *J. Chem. Phys.* **15,** 174–180 (1947).
26. Sickafus, K. E. *et al*. Cation disorder in high-dose, neutron-irradiated spinel. *J. Nucl. Mater.* **219,** 128–134 (1995).
27. Redfern, S. A. T., Harrison, R. J., O'Neill, H. S. C. & Wood, D. R. R. Thermodynamics and kinetics of cation ordering in $MgAl_2O_4$ spinel up to 1600 degrees C from *in situ* neutron diffraction. *Am. Mineral.* **84,** 299–310 (1999).
28. Asbrink, S., Waskowska, A., Olsen, J. S. & Gerward, L. High-pressure phase of the cubic spinel $NiMn_2O_4$. *Phys. Rev. B* **57,** 4972–4974 (1998).
29. Ivanov, V. G. *et al*. Short-range B-site ordering in the inverse spinel ferrite $NiFe_2O_4$. *Phys. Rev. B* **82,** 024104 (2010).
30. Jiang, C., Sickafus, K. E., Stanek, C. R., Rudin, S. P. & Uberuaga, B. P. Cation disorder in MgX_2O_4 (X = Al, Ga, In) spinels from first principles. *Phys. Rev. B* **86,** 024203 (2012).

Acknowledgements

We thank T. Egami, A. Fuentes and B. Haberl for discussions. This work was supported as part of the Materials Science of Actinides, an Energy Frontier Research Center funded by the US Department of Energy, Office of Science, Basic Energy Sciences under Award # DE-SC0001089. This research at ORNL's Spallation Neutron Source was sponsored by the Scientific User Facilities Division, Office of Basic Energy Sciences, US Department of Energy.

Author contributions

J.S., C.L.T., R.C.E. and M.L. conceived and designed the experiments. M.L. and C.L.T. designed and coordinated the irradiation procedure. J.S., F.Z., S.F., D.B. and H.Z. synthesized the samples. J.S., M.F., C.L.T., J.N. and M.L. collected and interpreted the neutron scattering data. J.S., C.L.T., R.C.E. and M.L. prepared the manuscript.

Additional information

Supplementary information is available in the online version of the paper. Reprints and permissions information is available online at www.nature.com/reprints. Correspondence and requests for materials should be addressed to M.L.

Competing financial interests

The authors declare no competing financial interests.

Methods

Two ordered pyrochlore compositions ($Ho_2Ti_2O_7$, $Er_2Sn_2O_7$) and isometric spinel ($MgAl_2O_4$) were synthesized via conventional solid-state methods. Ordered $Nd_2Zr_2O_7$ was prepared by a wet chemical synthesis technique. Aqueous solutions of $ZrOCl_2 \cdot 8H_2O$ and $Nd(NO_3)_3 \cdot 6H_2O$ were prepared and mixed in stoichiometric ratios. Hydroxides were co-precipitated in 25% concentrated liquid ammonia (NH_4OH). This process is described in detail by Finkeldei and colleagues[31]. Disordering was achieved in the pyrochlore compounds by varying the chemical composition during solid-state synthesis ($Ho_2Zr_2O_7$, $NiAl_2O_4$), altering the stoichiometry during wet chemical synthesis ($Nd_{0.94}Zr_{2.53}O_{6.47}$), and irradiation with 2.2 GeV ^{197}Au ions ($Er_2Sn_2O_7$), respectively.

The as-prepared $Er_2Sn_2O_7$ powder was pressed into four custom-made aluminium sample holders (indented circular area of 1 cm diameter and 75 µm depth) and irradiated to an ion fluence of 8×10^{12} ions cm^{-2} at the X0 beamline of the GSI Helmholtz Centre for Heavy Ion Research in Darmstadt. The beam energy was sufficiently high for all Au ions to completely pass through the 75-µm thick sample pellets with a near-constant electronic energy loss per unit path length ($dE/dx = 23.7 \pm 0.4$ keV nm^{-1}). The ion range (107 µm) and the dE/dx were determined using the SRIM code[32] with a powder packing fraction of 0.5. After irradiation, the ~100 mg powder was removed from the Al holders and inserted into quartz capillaries with an outer diameter of 2 mm and wall thickness of 0.01 mm.

Structural characterization was performed at the Nanoscale-Ordered Materials Diffractometer (NOMAD) at the Spallation Neutron Source at Oak Ridge National Laboratory. Approximately 100 mg of each sample was measured in 2 mm diameter quartz capillary cans for 90 min at room temperature. NOMAD detectors were calibrated using scattering from diamond powder and standard Si powder was measured to obtain the instrument parameter file for the Rietveld refinements. The highest Q-resolution backscattering bank was used for the Rietveld refinements of the diffraction data. To obtain the structural factor $S(Q)$, the scattering intensity was normalized to the scattering from a solid vanadium rod and background was subtracted using an identical, empty 2 mm quartz capillary can measured for the same time as the powder samples. The pair distribution function (PDF) was calculated by the Fourier transform of $S(Q)$ with $Q_{min} = 0.1$ Å^{-1} and $Q_{max} = 31.4$ Å^{-1}:

$$G(r) = \frac{2}{\pi} \int_{Q_{min}}^{Q_{max}} Q[S(Q) - 1] \sin(Qr) dQ \qquad (1)$$

where Q is the scattering vector, defined as $Q = 4\pi/\lambda \sin\theta$, and λ and θ are the neutron wavelength and scattering angle, respectively. The PDFs were characterized with small-box refinement (discussed below).

Rietveld refinements of diffraction data were completed using FullProf (https://www.ill.eu/sites/fullprof). All PDF refinements were carried out using the PDFgui software[33]. A total of five refinement parameters were used when refining the PDF using the isometric, disordered fluorite model ($Fm\bar{3}m$). These included the unit cell parameter ($a = b = c$), the scale factor, the correlated motion parameter (PDF refinements), and one atomic displacement parameter (ADP) ($u11 = u22 = u33$) for each crystallographic site. Because both cations share crystallographically equivalent sites, a single ADP was used for both the A- and B-site cations, whereas a second ADP was used for the oxygen anion sites. In this model, A- and B-site cations equally share full occupancy of 4*a* sites (0, 0, 0), whereas oxygen anions occupy 7/8ths of the 8*c* sites (0.25, 0.25, 0.25). Owing to the isometric structure and fixed Wyckoff sites, no more than five parameters can be refined.

The number of PDF refinement parameters was increased to 12 for the pyrochlore structure ($Ho_2Ti_2O_7$, $Fd\bar{3}m$): unit cell parameter ($a = b = c$), scale factor, correlated motion parameter (PDF refinements), x-position for 48*f* sites, and eight ADPs. The eight ADPs include two each for 16*c* and 16*d* sites ($u11 = u22 = u33$ and $u12 = u13 = u23$), three for 48*f* sites ($u11 \neq u22 = u33$ and $u23$), and one for 8*b* sites ($u11 = u22 = u33$).

Refinement of the PDF using the orthorhombic, weberite-type model ($Ccmm$) required a total of 28 restraints. These included three unit cell parameters ($a \neq b \neq c$), scale factor, correlated motion parameter (PDF refinements), eight atomic position parameters, and 15 ADPs. The eight position parameters are comprised of the x- and y-position for 8*g* sites, the x-, y-, and z-positions for 16*h* sites, and the x-position for all three 4*c* sites. For simplicity, each Wyckoff site was given its own set of three ADPs ($u11 \neq u22 \neq u33$). In other words, all 4*a* sites had their own $u11$, $u22$, and $u33$; all 4*b* sites then had a different $u11$, $u22$, $u33$ and so on. The three 4*c* sites were given the same set of ADPs. All refinements resulted in no highly correlated constraints.

A total of 23 refinement parameters were used for PDF refinement of the tetragonal spinel ($P4_122$) phase in $NiAl_2O_4$. These included two unit cell parameters ($a = b \neq c$), the scale factor, the correlated motion parameter (PDF refinements), the 'inversion' parameter, nine position parameters, and nine ADPs. The inversion parameter, i, was defined as the fraction of 4*a* sites occupied by nickel (or the fraction of 4*c* sites occupied by Al) and was used to calculate the site occupancies (4*b* sites were fully occupied by Al). The position parameters included $x = y$ for 4*c* sites, y for 4*a* and 4*b* sites, and x, y and z for both 8*d* (oxygen) sites. Each cation site had its own ADP ($u_{11} = u_{22} = u_{33}$), whereas each 8*d* site had three ADPs ($u_{11} \neq u_{22} \neq u_{33}$). The above procedure was also used for $MgAl_2O_4$.

Only eight refinement parameters could be used for refining the isometric spinel phase for $NiAl_2O_4$ ($Fd\bar{3}m$), including the unit cell parameter ($a = b = c$), the scale factor, the correlated motion parameter (PDF refinements), the inversion parameter, 32*e* (oxygen) position parameter ($x = y = z$), and three ADPs. Each Wyckoff site (8*a*, 16*d*, 32*e*) was given its own ADP ($u_{11} = u_{22} = u_{33}$). The inversion parameter, i, denoted the fraction of 8*a* sites occupied by Al (the fraction occupied by Ni was therefore $1 - i$). The fraction of 16*d* sites occupied by Ni and Al was $i/2$ and $1 - i/2$ respectively. The above procedure was also used for $MgAl_2O_4$.

References

31. Finkeldei, S. *et al*. Dissolution of ZrO_2 based pyrochlores in the acid pH range: a macroscopic and electron microscopy study. *Appl. Geochem.* **49,** 31–41 (2014).
32. Ziegler, J. F., Ziegler, M. D. & Biersack, J. P. SRIM—The stopping and range of ions in matter (2010). *Nucl. Instrum. Methods Phys. Res. B* **268,** 1818–1823 (2010).
33. Farrow, C. L. *et al*. PDFfit2 and PDFgui: computer programs for studying nanostructure in crystals. *J. Phys. Condens. Matter* **19,** 335219 (2007).